Thermal Ring-Based Heat Switches in Hyperthermophilic Class II Bacterial Fructose Aldolase

Guangyu Wang*

ABSTRACT: Both thermophilic and hyperthermophilic enzymes in bacterial and archaeal species are activated above a specific temperature threshold but inactivated at another higher temperature. However, the underlying structural basis for these two heat switches is still unresolved. Here, graph theory was used to test if the temperature-dependent noncovalent interactions and metal bridges as identified in a series of crystal structures of the class II bacterial fructose 1,6-bisphosphate aldolase homodimer or homotetramer with or without natural substrates and products bound could form systematic fluidic grid-like mesh networks with topological grids as thermal rings to regulate their structural thermostability and functional thermoactivity. The results indicated that the second biggest grid in the *Thermus aquaticus* fructose 1,6-diphosphate aldolase dimer may control the specific temperature threshold to release the swapping flexible active sites at the dimeric interface for heat-evoked activation. Meanwhile, the third biggest grid may serve as a necessary structural motif against heat inactivation. Finally, the smallest grid may act as a stiff thermostable anchor. Its dissociation at the maximal melting temperature threshold may stop the catalytic activity. Taken as a whole, this computational study may render the structural motifs for the optimal growth temperature and the extreme heat stability of hyperthermophiles.

INTRODUCTION

The activity of thermophilic and hyperthermophilic enzymes in bacterial and archaeal species is highly temperature-dependent. They generally do not function well until above 40 °C. The former has usually optimal activity in a range from 60 to 80 °C, while the latter generally has high thermostability and optimal catalytic activity at temperatures above 70 °C but some are active at temperature as high as 110 °C or above.[1] A representative is the thermostable metal-dependent class II *Thermus aquaticus* fructose 1,6-diphosphate aldolase (TaA) that reversibly cleaves its ketohexose substrate into triose phosphates during gluconeogenesis, the Calvin cycle, and glycolysis.[2] This enzyme exhibits little activity at temperatures below 60 °C and optimal activity at about 95 °C in the presence of NH_4^+ and Co^{2+} or Fe^{2+} or Zn^{2+}.[2] Owing to a high degree of sequence and structural homology between hyperthermophilic and mesophilic globular proteins, the delicate balance of the noncovalent interactions such as salt bridges in these two classes of proteins has been proposed as the source of this extreme thermal tolerance.[3] However, much less is known about how these noncovalent interactions work together as the structural motifs to achieve the optimal growth temperature and extreme heat stability even if the relevant crystal structures have been available at room temperatures for some proteins.

Thermal unfolding of protein structures has been simulated by using the graph theory-based network analysis of main noncovalent interactions such as salt bridges and hydrogen bonds.[4−9] Although those approaches are useful to indicate flexible and rigid regions or the interaction strength distributions of mesophiles and thermophiles, the relevant accuracy is not enough to account for the increased thermostability and thermoactivity of thermophilic enzymes completely. For example, the rigid theory-based constraint network analysis (CNA) by removing noncovalent interactions one by one, from the weakest to the strongest according to energy ranking, only allowed the differences in computed phase-transition temperatures (T_p) between a mesophilic protein and its thermophilic homologue to be roughly comparable to the differences in experimental optimal growth temperatures.[6] On the other hand, the performance of residue interaction networks (RINs) with energy weighted only permits to distinguish thermostable and mesostable proteins with an accuracy of 76%.[9] Therefore, other structural factors need to be included to improve the prediction accuracy for better thermostability engineering.

Recently, following the findings that the melting temperature threshold (T_m) of an intramolecular DNA hairpin in a single polynucleotide chain is determined by not only the number of H-bonds in the stem but also the loop length,[10] a graph theory-based grid thermodynamic model has been developed to corroborate the network basis for the temperature-dependent

Table 1. Noncovalent Interactions in Monomers A and B of Native TaA

noncovalent interaction	cutoff distance	linked residues
salt bridge	3.2–4 Å	K103-E114, R116-E120, D190-R193, D253-R257, D255-R295, E286-K289
H-bond	<3.9 Å	K11-Y17, N23-D80, Q31-R285, E35-K289, E39-K289/K293, S42-S301, E50-S83/S87, E66-K69, H78-S98-Y169-T128, S84-E86, D102-S104, D107-T110, E109-R164, N111-T115, H123-D168, E130-H208, H191-D238, R220-E266, and D276-R278
$\pi-\pi$ interaction	2.65–6.5 Å	F29-F260, F108-F161
cation-π interaction	<6.0 Å	Y85-R117
CH$_3$/CH-π interaction	2.65–3.01 Å	L9-Y169, Y17-R304, F22-V292, V77-F96, L133-F161-T165, H191-K241, F221-L258, I250-F299

structure−function relationships of class I fructose bisphosphate (FBP) aldolase B and class II *E.coli* FBP aldolase.[11,12] Generally speaking, when noncovalent interactions along a single polypeptide chain form a systemic fluidic grid-like mesh network, the melting temperature threshold to start the structural or functional perturbation of a biological macro-molecule is determined not only by the energy intensity and the number of unique noncovalent interactions in the available biggest grid but also the size of the grid sealed by those noncovalent interactions.[11,12] Further, the low systematic thermal instability (T_i) is also theoretically and experimentally in good accord with the higher temperature thresholds for the structural thermostability of those two classes of FBP aldolases,[11,12] providing support and validation of this novel graphical approach. In this regard, such a simple but powerful grid thermodynamic model not only has gone beyond describing proteins as topological networks but also unexpectedly integrated multiple factors such as the intensity of noncovalent interactions, cluster sizes, core packing, cavity volumes, and packing density into crucial topological grids as determinant thermal rings for the structural thermostability and the functional thermoactivity of biomacromolecules and for relevant biotechnological applications of protein engineering in industry. In order to further examine this model independently and to evaluate its potential in predicting the activity threshold range of thermosensitive proteins *ab initio*, it is intriguing to test if the melting of the available biggest grids in a systematic fluidic noncovalent interaction mesh network be responsible for thermal activation and inactivation of hyperthermophilic TaA.

In this *in silico* study, graph theory was used to examine this hypothesis by carefully pinpointing grids one by one, from the biggest to the smallest, in the systematic fluidic grid-like noncovalently interacting mesh networks as identified in the crystal structures of the native class I TaA homotetramer at 295 K.[13] When the melting temperature threshold (T_m) of a candidate grid was calculated as close to the measured threshold for thermal activation above 60 °C, starting inactivation at about 95 °C, or no activity at 113 °C, two biggest grids and the smallest one were subsequently identified to link the crystallographic static conformation with the functional activity in atomic details. While the third biggest grid may serve as a necessary structural motif to avoid thermal inactivation below the calculated melting temperature threshold 94 °C, the second biggest grid near the dynamic flexible metal-dependent active site may play a critical switching role in heat-evoked activation of this hyper-thermophilic isoenzyme. Once the smallest stiff anchor grids were dissociated or decayed, a loss of catalytic activity may happen to TaA. Thus, both classes I and II fructose aldolases, although have different catalytic mechanisms, may need a rigid anchor grid for the structural thermostability and a dynamic

flexible active site for the functional thermoactivity. Their balance may result in an optimal activity temperature.

■ MATERIALS AND METHODS

Data Mining Resources. In this computational study, the high-resolution X-ray crystallographic structures of several homologous class II bacterial FBP aldolases or the relevant mutant in the presence or absence of $(NH_4)_2SO_4$ at room temperature were selected as data mining resources. They included sulfate-bound TaA (PDB ID, 1RVG; model resolution = 2 Å), ligand-free *Helicobacter pylori* FBP aldolase (HpA) (PDB ID, 3C4U; model resolution = 1.83 Å), HpA with dihydrox-yacetone phosphate (DHAP) bound (PDB ID, 5VJF; model resolution = 1.85 Å), HpA with DHAP and glyceraldehyde-3-phosphate (G3P) bound (PDB ID, 5UCK; model resolution = 1.782 Å), HpA-H180Q with FBP bound (PDB ID, 5UD3; model resolution = 1.44 Å), *Bacillus anthracis* FBP aldolase (BaA) with DHAP bound (PDB ID, 3Q94; model resolution = 2.3 Å), *Escherichia coli* FBP aldolase (EcA) with D-glucitol-1,6-bisphosphate (GBP) bound (PDB ID, 5VJE; model resolution = 1.65 Å), and *Mycobacterium tuberculosis* FBP aldolase (MtA) with FBP bound (PDB ID, 3ELF; model resolution = 1.31 Å).[13−17] They were analyzed with graph theory to uncover the thermal ring-based melting temperature threshold (T_m) parameters for the heat switches in TaA.

Standards for Noncovalent Interactions. A previous study showed that small structural differences induce large fluctuations in the computed clusters.[7] Hence, the same stringent standard definition of noncovalent interactions as described previously was employed to secure the resultant grid and its size being reproduced with a high sensitivity (Table 1).[11,12] To this end, the structure visualization software, UCSF Chimera, was used to filter stereo- or regioselective interdomain diagonal and intradomain lateral noncovalent interactions in the isoenzymes as mentioned above and to examine their potential roles in shaping topological grids with minimal ring sizes to govern the T_m for the heat-evoked activity changes from a start to a peak and then to an end. Those noncovalent interactions included salt bridges, cation/CH/$\pi-\pi$ interactions, and H-bonds along the single polypeptide chain from L9 to R304 (Table 1).

Preparation of Topological Grid Maps by Using Graph Theory. With all of the noncovalent interactions and the metal bridges along the single polypeptide chain from L9 to R304 being filtered according to the above stringent standard (Table 1), they were mapped as edges in the whole systematic fluidic topological grid-like mesh network along with vertices for the positions of the linked amino acid residues, which were marked as node arrows. All of the grids were then included in this network after their ring sizes were constrained as the minimal
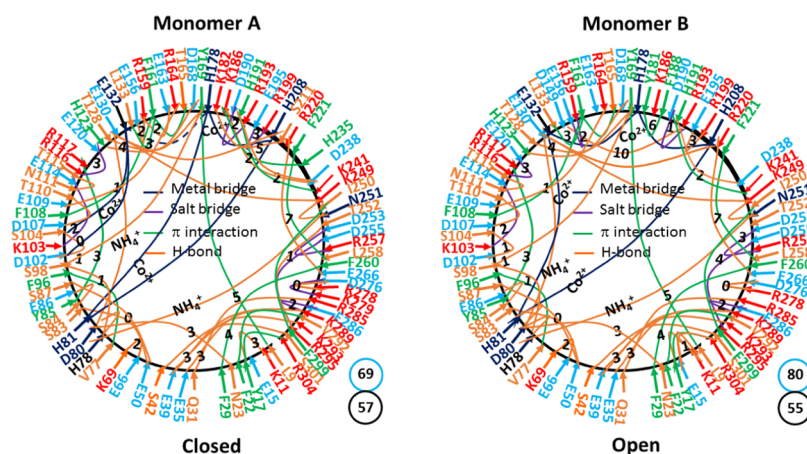
Figure 1. Topological grids in the systemic fluidic grid-like noncovalently interacting mesh network along the single polypeptide chain of the sulfate-bound native class II TaA homotetramer at 295 K. The X-ray crystallographic structures of monomers A and B in the dimer of the wild-type class II TaA homotetramer with sulfate bound at 295 K (PDB ID, 1RVG) were used for the model. Salt bridges, metal bridges, π interactions, and H-bonds between pairing amino acid side chains along the single polypeptide chain from L9 to R304 are marked in purple, dark blue, green, and orange, respectively. The grid sizes required to control the relevant noncovalent interactions and metal bridges were calculated with graph theory and are labeled in black. The total grid sizes and grid size-controlled noncovalent interactions and metal bridges along the single polypeptide chain are shown in the blue and black circles, respectively.
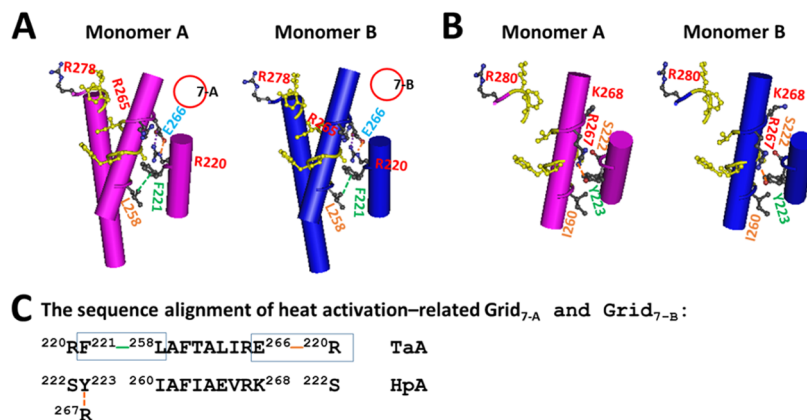
Figure 2. Structural comparison of the network grid-based heat switches for thermal activation. (A) Structures of switch-off Grid$_{7-A}$ in monomer A and Grid$_{7-B}$ in monomer B. The grid sizes S_{max} are shown as the first numbers in red circles. The X-ray crystallographic structures of monomers A and B in the dimer of the wild-type class II TaA homotetramer at 295 K (PDB ID, 1RVG) were used for the model. (B) Structures of broken Grid$_{7-A}$ in monomer A (pink) and Grid$_{7-B}$ in monomer B (blue) in native HpA for thermal activation. The X-ray crystallographic structures of monomers A and B in the ligand-free class II HpA homodimer at 293 K (PDB ID, 3C4U) were used for the model. (C) The sequence alignment of heat activation-related Grid$_{7-A}$ and Grid$_{7-B}$ between class II TaA and HpA. The controlled R220-E266 H-bond and the F221-L258 π interaction in Grid$_{7-A}$ and Grid$_{7-B}$ are shown in blue boxes. R267 H-bonded with Y223 in HpA.

number of the total free silent side chains of residues, which did not engage in any noncovalent interaction or metal bridge in the grid. The size constraint was done by using graph theory and the Floyd–Warshall algorithm to calculate the shortest return path between two residues linked by the noncovalent interaction, which resulted in the direct path as zero.[18] For example, in the biochemical reaction network of monomer A or B in Figures 1 and 2, the direct path length from R220 and E266 was zero because of an H-bond between them. However, another shortest return path existed from E266 to R220 via the segment ^{265}RILATFA^{259} and the L258-F221 π bridge in this grid. When the length of that free segment not involving any noncovalent interaction or metal bridge in the grid was 7 residues, the grid size was then 7. After each noncovalent interaction together with metal bridges was tracked by a specific grid size, the unshared sizes were marked in black. Usually, a grid with an x-residue size in monomer A or B was denoted as Grid$_{x-A}$ or Grid$_{x-B}$,

respectively. In so holding, the total grid sizes and the total noncovalent interactions and metal bridges along the single polypeptide chain were shown in black and blue circles beside the mesh network map for the calculation of the systematic thermal instability.

Equations. For a DNA hairpin thermosensor with a 20 bases long poly-A loop and two G-C base pairs in the stem, a start control melting temperature threshold (T_m) to initiate thermal unfolding of the hairpin loop is 34 °C. The T_m is raised by 10 °C along with an increase in five additional bases in the loop or one additional G-C base pair in the stem.[10] Similarly, when a single polypeptide chain in protein undergoes rate-limiting thermal unfolding of the thermal rings from the biggest grid to the smallest grid, the T_m of thermal unfolding of the given grid along the chain was calculated by using the following equation as described previously[11,12]

$$T_m(°C) = 34 + (n - 2) \times 10 + (20 - S_{max}) \times 2 \qquad (1)$$

where n is the total number of H-bonds energetically equivalent to the noncovalent interactions controlled by the given grid and S_{max} is the size of the given grid. In this regard, decreasing grid size or increasing equivalent H-bonds will increase the grid's heat capacity.

On the other hand, the more the G-C base pairs in the stem or the shorter the poly-A loop, the higher the T_m of the DNA hairpin.[10] In this regard, the grid-based systemic thermal instability (T_i) along the single polypeptide chain was reasonably defined using the following equation as described previously[11,12]

$$T_i = S/N \qquad (2)$$

where S is the total grid sizes along the single polypeptide chain of one subunit in a functional state and N is the total noncovalent interactions and metal bridges along the same single polypeptide chain of one subunit in the same functional state. In so holding, the lower the T_i, the less the conformational entropy in the system.

■ RESULTS

Identification of the Biggest Grids in the Class II TaA Dimer at 295 K. Monomers A and B from the same primary sequence in the SO_4^{2-}-bound wild-type (WT) class II TaA dimer have closed and open conformers, respectively.[13] The dimeric interface had swapping E28-Y55′ and E70-R58′ and Y280-T261′ H-bonds, F221/L258-F275′ and Y55-R278′/R285′ π interactions, and D276-R257′ salt bridges.[13] In both conformers, a monovalent cation NH_4^+ H-bonded with H78, D80, E130, and N251, while K249 also H-bonded with N251 and E130.[13] On the other hand, H81, H178 and H208 formed a common Co^{2+} or Zn^{2+} bridge. Further, E132 linked with D102 and S104 in closed monomer A but with H81 and H178 in open monomer B via the Co^{2+} or Zn^{2+} bridge.[13] These bridges allowed the smallest resultant grids with a zero-residue size to participate in the active site during the catalytic cycle. Apart from those H-bonding and metal bridges, most of the noncovalent interactions were shared by both conformers along the single polypeptide chain from L9 to R304 (Table 1). They included 6 salt bridges, 12 π interactions, and 23 H-bonds (Table 1).

On the other hand, there were some different noncovalent interactions between amino acid side chains in two conformers.[13] For example, the D276-R279 salt bridge, the K159-E163 and K182-S211 and K186-D238 and T252-R295 H-bonds, and the K186-H235 π interaction were present in closed monomer A but absent in open monomer B (Figure 1). Meanwhile, the K11-E15-R304 and D80-H81 and D149-R193 H-bonds and the Y181-F188 π interaction were only shown in open monomer B. In addition, an exchange between H-bonds and salt bridges were found in both conformers for pairs E156-R159 and E195-R199 (Figure 1). These differences allowed closed monomer A and open monomer B to present distinct total noncovalent interactions together with metal bridges and total grid sizes as 57 and 69 for the former and 55 and 80 for the latter, respectively. Consequently, the systematic thermal instability (T_i) values were 1.21 and 1.45 for monomers A and B of the WT construct, respectively (Table 2). In addition to those differences, the grid size ranged from 0−7 in closed monomer A but 0−10 in open monomer B (Figure 1). The first biggest $Grid_{10}$ was only shown in open monomer B, but the second biggest $Grid_7$ was seen in both conformers (Figure 1).

Table 2. Grid Thermodynamic Model-Based New Parameters of Native TaA

construct	TaA					
monomer	A	B	A	B	A	B
grid #	7-A	7-B	5-A	5-B	0-A	0-B
S_{max}, a.a	7	7	5	5	0	0
equivalent H-bonds for S_{max}	2	2	5	5	6	6
calculated T_m, °C	60	60	94	94	114	114
measured T_{th}, °C	60	60	95	95	113	113
S	69	80	69	80	69	80
N	57	55	57	55	57	55
T_i	1.21	1.45	1.21	1.45	1.21	1.45
reference	2	2	2	2	2	2

Melting of the Second Biggest $Grid_{7-A}$ and $Grid_{7-B}$ Was Required for Thermal Activation above the Calculated T_m of 60 °C. If the melting of the first biggest $Grid_{10}$ in open monomer B is required for thermal activation of native TaA, closed monomer A with the broken $Grid_{10}$ at room temperature 295 K should exhibit activity. However, no activity was observed at 22 °C.[2] Therefore, the first biggest $Grid_{10}$ may not be the candidate for the heat-evoked activation of this isoenzyme. In contrast, the second biggest $Grid_{7-A}$ in closed monomer A was also found as $Grid_{7-B}$ in open monomer B (Figure 2A). Both had a 7-residue size via the shortest path from R220 to F221 in the α8 helix, L258, E266 in α11 helix, and back to R220 to govern the R220-E266 H-bond and the F221-L258 π interaction (Figure 2C). When two equivalent H-bonds sealed $Grid_{7-A}$ and $Grid_{7-B}$, the calculated melting temperature threshold (T_m) was about 60 °C, which was exactly the same as the experimental activation threshold (T_{th}) of 60 °C (Table 2).[2]

If $Grid_{7-A}$ and $Grid_{7-B}$ were responsible for the heat-evoked activation above 60 °C, their disassociation at room temperature should allow the corresponding aldolase to be activated. In agreement with this assumption, when R220, F221, L258, and E266 in native TaA were replaced by S222, Y223, I260, and K268 in WT HpA, respectively, the new Y523-R267 H-bond prevented the formation of a π interaction between Y223 and I260 or an H-bond between S222 and K268 so that both $Grid_{7-A}$ and $Grid_{7-B}$ were broken at room temperature 293 K (Figure 2B). Meanwhile, this construct does have the catalytic activity at the same temperature, and the loop closures in the closed monomer A facilitate the activity-related relocation of the catalytic Zn^{2+} ion from its buried site I to the surface-exposed site II.[14] Therefore, the melting of both $Grid_{7-A}$ and $Grid_{7-B}$ may be required for heat-evoked activation of native class II TaA.

Basic Dimeric Cyclization upon the Swapping S49-R280′ H-bonds Was Required for the Catalytic Reactions in HpA. The highly conserved residue R331 in the class II EcA plays a very important role in C6-phosphate binding of FBP during the catalytic cycle reactions.[19,20] Thereafter, it is necessary to examine the effects of broken $Grid_{7-A}$ and $Grid_{7-B}$ on the conserved catalytic residues R278 in TaA and R280 in HpA. The structural comparison between homologous TaA and HpA indicated that broken $Grid_{7-A}$ and $Grid_{7-B}$ released the structural motif $^{280}RKF^{282}$ from the α10 helix in HpA, allowing the side chain guanidinium group of the critical residue R280 (R331 in EcA) to be flexible (Figure 2B). Further, in between α10 and α11′ of ligand-free HpA, the swapping I263-F282′ and F277′-I260 π interactions at the dimeric interface linked two active sites in monomers A and B together. However, S49 was separate from R259 from the same subunit and R280′ from the
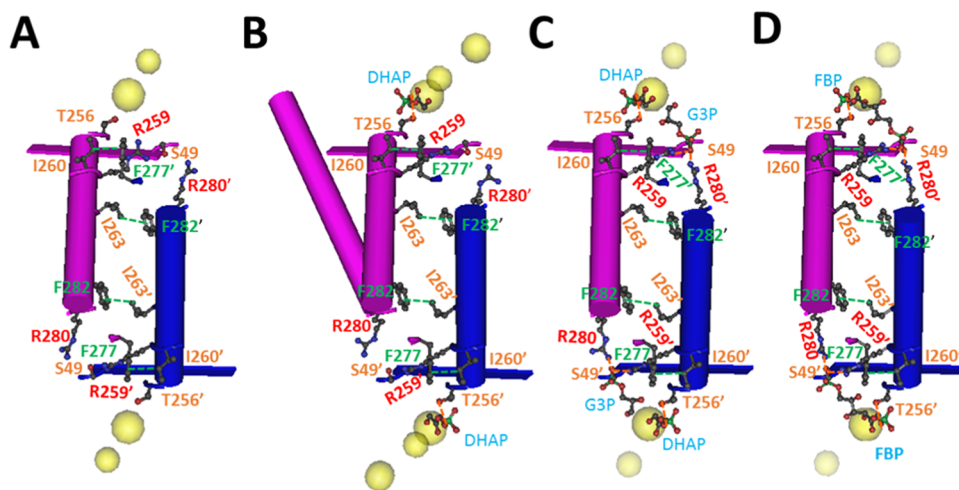
Figure 3. Structural comparison of the swapping noncovalent interactions at the dimeric interface to form the basic dynamic cyclization for the catalytic reactions. The X-ray structures of monomers A (pink) and B (blue) of the cryotrap reaction intermediates in the crystalline states of the class II HpA or HpA-H180Q homodimer at 293 K were used for the models. (A) WT apo-HpA (PDB ID, 3C4U); (B) WT HpA with DHAP bound (PDB ID, 5VJF); (C) WT HpA with DHAP and G3P bound (PDB ID, 5UCK); and (D) HpA-H180Q with FBP bound (PDB ID, 5UD3). The bigger spheres are monovalent cations such as K^+ or Na^+, while the smaller ones are divalent metal ions such as Zn^{2+}.
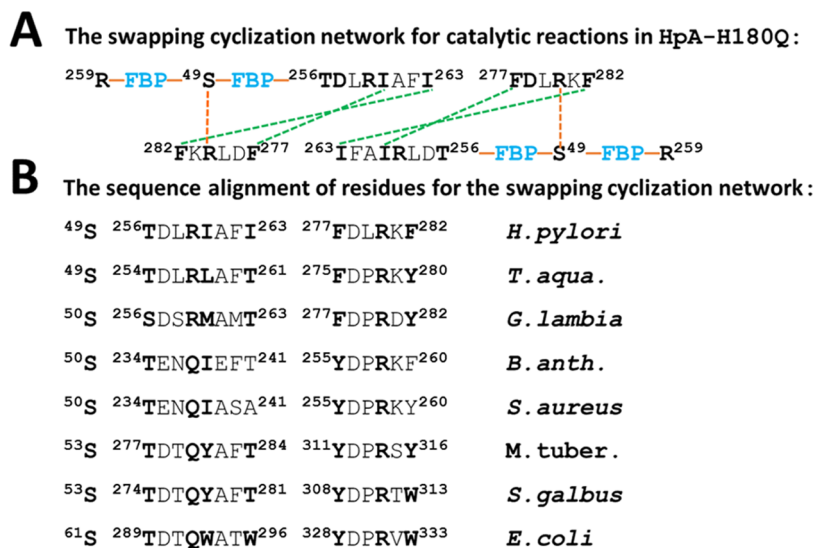
Figure 4. Sequence alignment of residues for swapping interfacial noncovalent interactions. (A) Swapping cyclization network for catalytic reactions in HpA-H180Q. (B) Sequence alignment of residues for the swapping cyclization network at the dimeric interface.

interfacial partner subunit (Figure 3A). The similar separation was also found when DHAP was bound to Co^{2+} or Zn^{2+} at the active sites, and its phosphate group H-bonded with T256 from the same subunit (Figure 3B). However, in the presence of DHAP and G3P together, the phosphate group of G3P H-bonded with not only the side chains of S49 and R259 from the same subunit but also the side chain guanidinium group of R280′ from the interfacial partner subunit (Figure 3C). The similar H-bond network was also observed when FBP was bound to the metal-dependent active sites in HpA-H180Q (Figure 3D). Hence, there were two kinds of swapping cyclization at the dimeric interface: one from F282 to I263′, I260′, and F277 and back to F282; the other from S49 to R280′, S49′, R280 and back to S49 via FBP (Figure 4A). These swapping interactions may enhance active site integrity against higher temperatures.

Further sequence alignment indicated that the key residues for CH−π interactions in these interfacial circles are highly conserved (Figure 4B).[14−17] However, the structural compar-

ison with the mesophilic counterparts showed no π interaction between T241 from one subunit and F260′ from the other in BaA (Figure 5A). A similar absence was also found between A241 and Y260′ of *S. aureus* FBP aldolase (Figure 4B). In contrast, swapping W296-W333′ π interactions in EcA with GBP bound, T284-Y316′ H-bonds in MtA with FBP bound, and T261-Y280′ H-bonds in TaA with a phosphate anion analogue sulfate bound were well conserved (Figure 5B−D). Despite this subtle difference, the swapping I238-Y255′ in BaA, W293-Y328′ in EcA, Y281-Y311′ in MtA, and L258-F275′ in TaA were conserved throughout the whole family (Figures 4B and 5). Thereby, this similar topology among the homologous enzymes may allow hyperthermophilic TaA to employ the same basic swapping cyclization for the catalytic reactions.

Grid$_{7-A}$ and Grid$_{7-B}$ Locked TaA in a Resting State below 60 °C. For TaA, the similar swapping T261-Y280′ H-bonds and L258-F275′ π interactions at the dimeric interface also constituted basic anchors, which may prime the catalytic
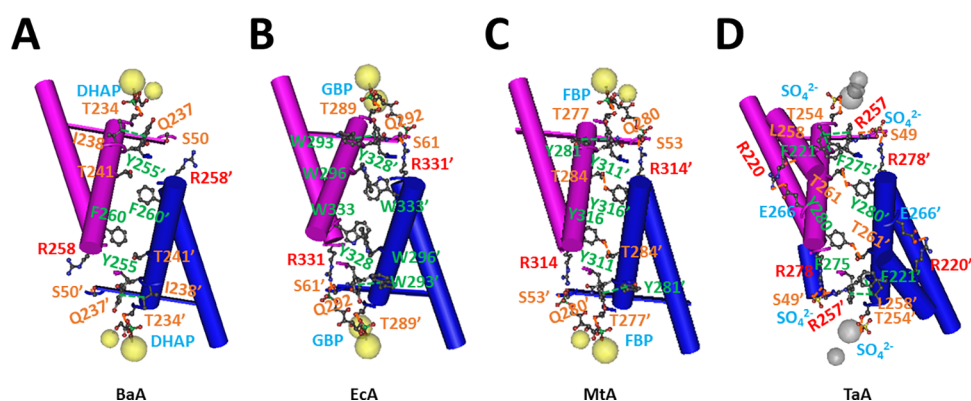
Figure 5. Structural comparison of the swapping noncovalent interactions at the dimeric interface to form the dynamic cyclization for the catalytic reactions. The X-ray crystallographic structures of monomers A (pink) and B (blue) in the dimer of class II BaA with DHAP bound (A), EcA with GBP bound (B), MtA with FBP bound (C), and TaA with a phosphate anion analogue SO_4^{2-} bound (D) at 293 K (PDB ID, 3Q94, 5VJE, 3ELF, and 1RVG, respectively) were used for the models. The bigger spheres could be monovalent cations K^+ or Na^+ or NH_4^+, while the smaller ones could be divalent metal ions such as Zn^{2+} or Co^{2+}.
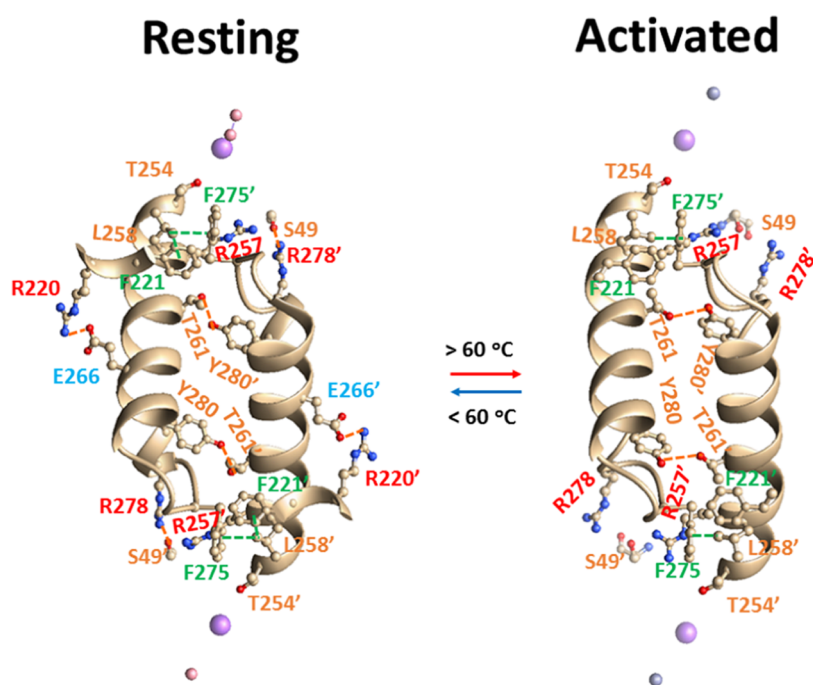
Figure 6. Tentative model for the heat activation-related switch at the dimeric interface for catalytic reactions in TaA. The X-ray crystallographic structures of monomers A and B in the wild-type class II TaA homotetramer (PDB ID, 1RVG) and the HpA homodimer (PDB ID, 3C4U) at room temperature were used for the models from a resting state into a catalytically active-state above a heat threshold 60 °C. The smaller spheres are Co^{2+} while the larger ones are NH_4^+. The dynamic flexible side chain guanidinium groups of R278 residues above 60 °C are required for spacious active sites to hold natural substrates and products stably during the catalytic cycle reactions. However, Grid$_{7-A}$ and Grid$_{7-B}$ locked the dynamic flexible side chain guanidinium group of R278 in a rigid α-helix below 60 °C, switching off the activation.

reactions near the metal active sites. On the other hand, the *in silico* modeling based on the ligand-free HpA showed that the dynamic flexible side chain guanidinium group of the critical conserved residue R278 may be required to hold natural substrates and products such as FBP or DHAP plus G3P with variable sizes in favor of such a significant extrapolation in reaction space and a nearby conformational change for the relocation of the Zn^{2+} cofactor 4Å from its interior site I to the surface-exposed site II during the catalytic cycle reactions (Figure 6).[17] However, in the presence of the L258-F221 π interactions and the R220-E266 H-bonds in Grid$_{7-A}$ and Grid$_{7-B}$, the rigid motif ^{278}RKY^{280} in the α-helix may prevent the induced fit of the substrate and the relevant product between the divalent

metal ions or NH_4^+ from one subunit and the side chain guanidinium group of R278 from the interfacial one along with the relocation of the metal sites, thereafter locking native TaA in a resting state below 60 °C (Figures 2, 3, 5, 6). Thus, TaA may exploit the subtle differences in the dynamic binding affinity of the substrates and the product to create a thermodynamic switch for the catalytic reaction cycle.

Melting of the Third Biggest Grid$_{5-A}$ and Grid$_{5-B}$ Started the Thermal Inactivation above a Calculated T_m of 94 °C. Previous studies indicated that some biggest grids before Grid$_{11}$ in class I FBP aldolase B or Grid$_{9-2-A}$ and Grid$_{9-2-B}$ in class II *E. coli* FBP aldolase are responsible for the melting temperature threshold to initiate thermal inactivation.[11,12]
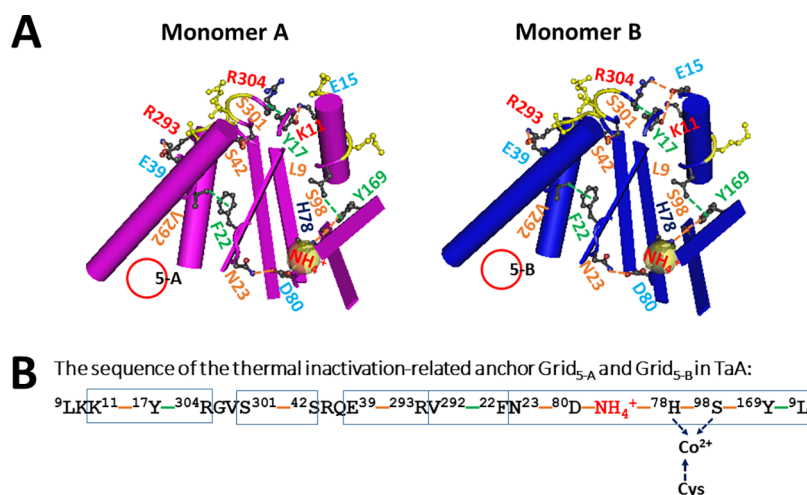
Figure 7. Structures of thermosensitive grids in the systemic fluidic grid-like mesh networks of native sulfate-bound class II TaA homotetramer at 295 K. The X-ray crystallographic structures of monomers A and B in the dimer of the wild-type class II TaA homotetramer with sulfate bound at 295 K (PDB ID, 1RVG) were used for the model. (A) Structures of thermosensitve $Grid_{5-A}$ in monomer A and $Grid_{5-B}$ in monomer B. The grid sizes S_{max} are shown as the first numbers in red circles. (B) Sequences of thermosensitive $Grid_{5-A}$ and $Grid_{5-B}$ to control the five equivalent H-bonds in blue boxes. External cystein is putatively linked with H78 and S98 via a Co^{2+} bridge.
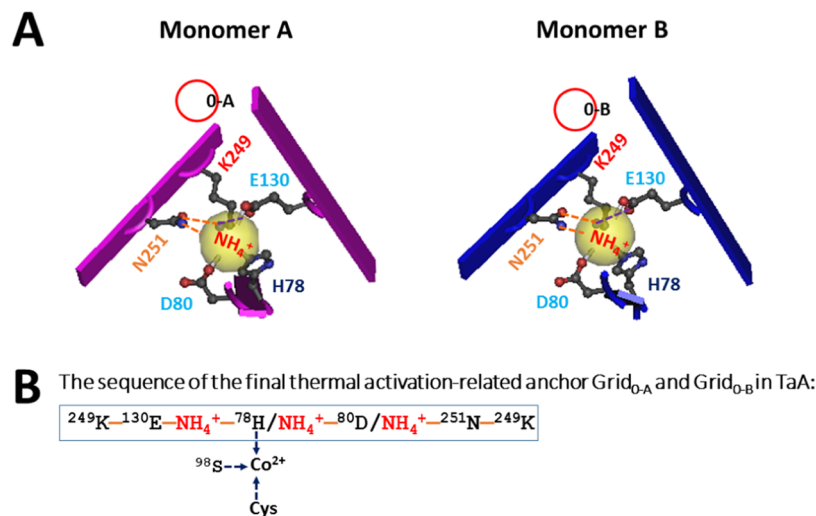
Figure 8. Structures of the final thermostable anchor grids in the systemic fluidic grid-like mesh networks of the native sulfate-bound class II TaA homotetramer at 295 K. The X-ray crystallographic structures of monomers A and B in the dimer of the wild-type class II TaA homotetramer with sulfate bound at 295 K (PDB ID, 1RVG) were used for the model. (A) Structures of the smallest thermostable anchors $Grid_{0-A}$ in monomer A and $Grid_{0-B}$ in monomer B. The grid sizes S_{max} are shown as the first numbers in red circles. (B) The sequences of thermostable $Grid_{0-A}$ and $Grid_{0-B}$ to control six equivalent H-bonds in the blue box. External cystein is putatively linked with H78 and S98 via the Co^{2+} bridge.

Similarly, the third biggest $Grid_{5-A}$ and $Grid_{5-B}$ were shown in closed monomer A and open monomer B of TaA, respectively (Figure 1). Both had a 5-residue size via the shortest path from L9 to K11, Y17, R304, S301, S42, E39, R293, V292, F22, N23, D80, NH_4^+, H78, S98, and Y169 and back to L9 (Figure 7). These two grids controlled five equivalent H-bonding pairs, including K11-Y17-R304, S42-S301, E39-R293, F22-V292, and N23-D80-NH_4^+-H78-S98-Y169-L9 (Figure 7). Thus, the calculated melting temperature threshold (T_m) was about 94 °C, which was close to the measured threshold 95 °C to start the thermal inactivation.[2]

Of special interest, the role of D82 in HpA (D80 in TaA) is limited to nothing but to keep active site integrity along with the substrate binding.[17] Therefore, it is reasonable that $Grid_{5-A}$ and $Grid_{5-B}$ may function as basic structural motifs against thermal inactivation between 60 and 94 °C. Once they are disassociated

or decayed above 94 °C, the TaA enzyme may start inactivation. Alternatively, the presence of external cysteine may form a putative Co^{2+} bridge with H78 and S98, reducing such a melting temperature threshold to 92 °C (Figure 7).[2]

Melting of the Smallest $Grid_{0-A}$ and $Grid_{0-B}$ Ended the Thermal Activity at a Calculated T_m of 114 °C. The previous studies also revealed that $Grid_{11}$ in class I FBP aldolase B and $Grid_{9-2-A}$ and $Grid_{9-2-B}$ in class II *E. coli* FBP aldolase are responsible for the melting temperature threshold to end the thermal activity.[11,12] Similarly, following the melting of $Grid_{5-A}$ and $Grid_{5-B}$, $Grid_{0-A}$ in monomer A and $Grid_{0-B}$ in monomer B became the final anchors to secure the thermal activation. They were the smallest grids in which NH_4^+ H-bonded with H78, D80, N251, and E130 in the presence of the N251-K249-E130 H-bonds (Figure 8). Since they had a zero-residue size and six equivalent H-bonds, the calculated T_m was about 114 °C, which
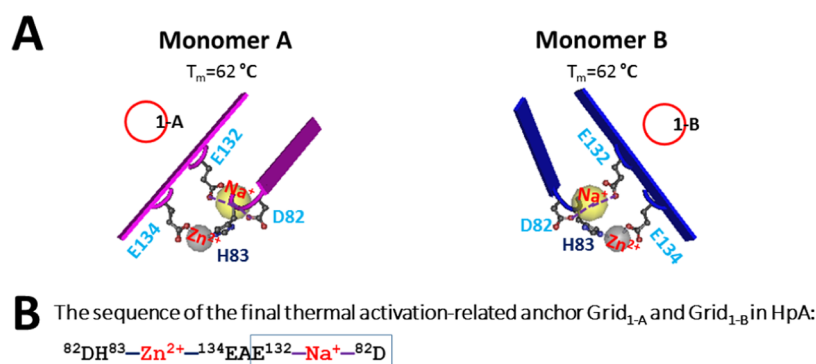
Figure 9. Structures of the final thermostable anchor grids in the systemic fluidic grid-like mesh networks of ligand-free native class II HpA homodimer at 293 K. The X-ray crystallographic structures of monomers A and B in the dimer of the wild-type class II apo-HpA homodimer at 293 K (PDB ID, 3C4U) were used for the model. (A) Structures of the smallest thermostable anchors $Grid_{1-A}$ in monomer A and $Grid_{1-B}$ in monomer B. The grid sizes S_{max} are shown as the first numbers in red circles. (B) Sequences of the thermostable $Grid_{1-A}$ and $Grid_{1-B}$ to control the E132-Na^+-D82 salt bridge in the blue box.

was near the measured T_{th} of 113 °C to end the thermal activation (Table 2).[2] Herein, D80 was shown again in $Grid_{0-A}$ and $Grid_{0-B}$ to maintain the active site integrity.[17] Therefore, when these two smallest anchor grids were broken at 114 °C, no activity would be observed. When external cysteine was introduced, it may form a putative Co^{2+} bridge with H78 and S98, disconnecting the H-bond between H78 and NH_4^+, hence decreasing the melting temperature threshold of $Grid_{0-A}$ and $Grid_{0-B}$ to 104 °C (Figure 8), which was exactly the same as the experimental value.[2]

In contrast, when Na^+ substituted NH_4^+ in HpA, the final thermoactivation-related $Grid_{1-A}$ in monomer A and $Grid_{1-B}$ in monomer B had a 1-residue size via the shortest path from D82 to H83, Zn^{2+}, E134, E132, and Na^+ and back to D82 (Figure 9). With one equivalent H-bond sealing these two grids to control the E132-Na^+-D82 salt bridge, the calculated melting temperature was about 62 °C. Thus, in the presence of K^+ or Na^+ but the absence of NH_4^+, it may be impossible to observe the catalytic activity for HpA above 62 °C. On the other hand, the calculated threshold for the thermal activation of TaA is about 60 °C above which the monovalent metal cation could not hold the anchor $Grid_{1-A}$ and $Grid_{1-B}$ intact (Figures 1, 2, and 9). That may be why TaA cannot be activated by K^+ or Na^+ at 80 °C.[2]

DISCUSSION

Class I and class II fructose aldolases catalyze the reversible adol condensation of DHAP with G3P to form FBP,[21] and both classes of enzyme have an overall characterized $(\beta/\alpha)_8$-barrel fold.[14] The class I enzymes in higher order organisms use a Schiff-base intermediate between the keto substrate (FBP or DHAP) and a lysine residue of the active site during catalysis. In contrast, class II enzymes in yeast, bacteria, fungi, and blue-green algae need a divalent metal ion (usually zinc or cobalt ion) as an electrophilic Lewis acid to stimulate aldol/retroaldol reactions by polarizing the keto carbonyl group of the substrate (FBP or DHAP) and stabilizing the enediolate intermediate during catalysis.[22] This computational study demonstrated that, although both classes of enzymes utilize different catalytic mechanisms, they both need a stiff thermostable anchor grid and a dynamic flexible active site to secure the catalytic reactions. Their balance may be responsible for the optimal activity temperature. Furthermore, a sequence alignment of class II bacterial fructose aldolases may help identify those respective structural factors or motifs.

Stiff Thermostable Anchor Grid in Each Monomer of the Class II TaA Homotetramer May Be Necessary to Secure Heat Activation. The thermostable anchors $Grid_{14}$ and $Grid_{11}$ have been reported in monomers D and A of class I aldolase B.[11] Since the calculated T_m range from 41 to 52 °C is consistent with the measured one from 40 to 50 °C,[11,23,24] both grids may serve as thermostable anchors to secure thermal activation below 40 °C. Further, $Grid_{11}$ is highly conserved throughout the three aldolase isozymes A, B, and C in class I.[25] Accordingly, the upper temperature limit for the activity of class I FBP aldolase may be 50 °C.

Following those findings, $Grid_{9-2-A}$ in monomer A and $Grid_{9-2-B}$ in monomer B of class II *E. coli* FBP aldolase were also identified as thermostable anchor grids to secure the final thermal activity from 55 °C for the native construct up to 66.9 °C for the evolved variants in the last generation. The increased threshold may be due to the enhanced strength of K25-N260 and Q18-T170 H-bonds in these two anchor grids upon the one-by-one generations.[12]

Similarly, once the smallest $Grid_{0-A}$ and $Grid_{0-B}$ allowed NH_4^+ and K249 to link H78, D80, E130, and N251 together via H-bonds (Figure 8), they had a zero-residue size and six equivalent H-bonds for the predicted melting threshold T_m of 114 °C to be close to the measured end threshold 113 °C for the final thermal activity (Table 2). In this regard, the maximal end temperature threshold of a hyperthermophilic enzyme could be at least 114 °C on the basis of the grid thermodynamic model. The maximal noncovalent interactions in the smallest grid may secure their long lifetime in the hyperthermophilic enzyme. What is more, with the replacement of NH_4^+ by K^+ or Na^+, the calculated melting temperature of $Grid_{1-A}$ and $Grid_{1-B}$ was about 62 °C (Figure 9). In that regard, it is reasonable that only NH_4^+ activates TaA at 80 °C.[2] If the R220-E266 H-bonds in $Grid_{7-A}$ and $Grid_{7-B}$ were broken (Figure 2), TaA would be activated at room temperature by not only NH_4^+ but also K^+ or Na^+.

Basic Dimeric Network-Based Flexible Catalytic Active Sites May Be Necessary for Heat-Evoked Activation. In addition to the rigid anchor $Grid_{11}$ in class I fructose aldolase, a dynamic flexible active site consisting of D33, R42, K107, K146, R148, E187, E189, K229, S271, and R303 has also been reported against $Grid_{11}$ and $Grid_{14}$ to realize the catalytic function in a temperature range of 10−50 °C for native class I aldolase B and 10−40 °C for the A149P mutant, respectively.[11,23,24] Thus, the graph theory-based grid thermodynamic model can be valid not

only at a high temperature 114 °C but also at a low temperature 10 °C. Of special note, both the dynamic flexible activate site and the anchor $Grid_{11}$ are located in the same subunit.

In contrast, when the strong rigid $Grid_{0-A}$ and $Grid_{0-B}$ in TaA function as thermostable anchors to secure thermal activation, it is a challenge to engineer a dynamic flexible metal-dependent active site in the same subunit to secure the catalytic activity. This computational study revealed that this kind of metal-loenzyme may exploit the final two helices, $\alpha 10$ and $\alpha 11'$, to form two kinds of basic dimeric interfacial swapping cyclization between two adjacent monomers to achieve this point. The first one used swapping F275-L258' and T261-Y280' bridges to stabilize the dimeric interface (Figures 3−6). When $Grid_{7-A}$ and $Grid_{7-B}$ were unfolded above 60 °C, the release of the structural motif $^{278}RKY^{280}$ from the α-helix may entail the positional plasticity of the side chain guanidinium group of R278 to form a structurally dynamic flexible space with S49 and R257 from the interfacial partner subunit in favor of the stable phosphate binding of DHAP plus G3P or FBP along the major axis of the ellipsoid of the Zn^{2+} ion for the catalytic cycle reactions. In this manner, concomitant conformational changes by active site loops allow not only the active site to be remodeled for the C−C bond cleavage but also the Zn^{2+} cofactor to be relocated in favor of its stabilization of the nascent enediolate species.[17] To this end, this proposal reinforces the crucial catalytic role of R331 in EcA during the catalytic cycle.[19,20] Since these two kinds of basic dynamic flexible swapping cyclization network are highly conserved in all class II FBP aldolases (Figures 4−5), the functional catalytic unit may be a dimer rather than a monomer as found in class I FBP aldolases. In support of this proposal, the introduction of cysteine increases the activity of TaA along with the presence of a dimer.[2] In contrast, the decyclization of this dimeric network by selective inhibitors may result in a loss of the catalytic activity of HpA.[26] Thus, these critical mechanistic insights into the role of the temperature-dependent dimeric cyclization in the catalytic reactions may lend alternative clues to class II aldolase-based drug design, protein engineering, and the industrial synthesis.

Structural Motifs for the Optimal Activity Temperature. On the other hand, the balance between the stiff thermostable anchor grids and the dynamic flexible active sites may be further regulated by $Grid_{5-A}$ and $Grid_{5-B}$ in a dimer-of-dimers of class II TaA (Figure 7). As they had the theoretical T_m of 94 °C close to the experimental 95 °C as the start temperature threshold for the thermal inactivation (Table 2), they may be necessary structural motifs to secure the catalytic activity at higher temperature. Based on the 5-residue size and two normal equivalent H-bonds in the grid, the T_m could be as high as 64 °C. Nevertheless, three additional equivalent H-bonds further increased the T_m up to 94 °C. That may be why the optimal activity temperature is about 95 °C.[2]

Of special note, D80 in $Grid_{5-A}$ and $Grid_{5-B}$ and $Grid_{0-A}$ and $Grid_{0-B}$ of TaA was also close the catalytic metal site (Figure 1). In this case, the presence of cysteine may form a putative Co^{2+} bridge with nearby H78 and S98, thus decreasing the start inactivation temperature threshold to 92 °C and the end one for the thermal activity to 104 °C while regulating the activity.[2]

Taken together, the balance between heat-evoked activation at a lower threshold and inactivation at a higher threshold may account for the diversified optimal activity temperatures of bio-macromolecule including enzymes from psychrophilic to mesophilic and hyperthermophilic. These increased optimal activity temperatures, 30 °C in class I FBP aldolase B, 43 °C in class II *E. coli* FBP aldolase, and 94 °C in class II TaA, are in good agreement with the decreased trend in their calculated systematic thermal instability (T_i) values in monomers A and B, 2.86−2.96, 2.56−2.72, and 1.21−1.45, respectively.[11,12] This decreased T_i may be required to absorb more heat as configurational heat capacity in the grids to minimize the conformational entropy compared to its mesophilic homologue for the same increase in temperature.

Once the balance is disrupted or shifted, the optimal activity temperature of protein against the thermal inactivation may change, either facilitating rational design of more durable variants in some enzymes like 2-deoxy-d-ribose-5-phosphate aldolase (DERA)[27] or causing some diseases such as the most popular cystic fibrosis as found in the F508-absent cystic fibrosis transmembrane conductance regulator (CFTR).[28−31]

Thermal Ring, from the Biggest Grid to the Smallest One, Is the Basic Structural Motif of a Biomacromolecule for the Thermal Activity. Furthermore, smaller conserved grids during the thermal titration may function as stable anchors or heat fuses to secure the thermal activation (Figures 7−9, Table 2).[11,12] The theoretical and experimental match in grid-based thresholds and systematic thermal instability showed that the thermal ring from the biggest grid to the smallest one is the basic structural motif for the bio-macromolecule to achieve the thermal activity (Figures 1−9, Table 2).[11,12] These thermal rings may play a critical role in absorbing more heat as configurational heat capacity to minimize a conformation entropy at elevated temperatures.[32] Although previous graph theory-based approaches including the RINs with energy weighted or the rigidity theory-based CNA have been used for the simulation of thermal unfolding of mesophiles and thermophiles or thermo-stability engineering, they failed to cover such determinant thermal rings to account for the whole activity temperature range from a start to a peak and then to an end.[4−9] In this regard, once a high-resolution 3D structure of protein is available for this graph theory-based grid analysis to include the thermal rings, the resultant grid thermodynamic model may allow scientists to have a whole topological picture of the thermoring structures in favor of rational and precise prediction and engineering design of the structural thermostability and the functional thermoactivity of a biological macromolecule.

■ CONCLUSIONS

This computational study investigated the thermoring basis for the heat-evoked activation and inactivation of class II TaA. The consistent theoretical and experimental temperature thresholds for those two events suggested that several biggest grids may in turn play critical roles in heat switches along with elevated temperatures. The melting of the second biggest grids may be required to switch on the catalytic activity while the disassociation of the third ones may initiate thermal inactivation. Of special interest, the final smallest anchor grids may be responsible for the upper temperature limit to active TaA. Thus, the basic thermal structure of a bio-macromolecule could be constrained as a series of thermal rings from the biggest grid to the smallest one. The thermal titration from a low temperature to a higher one allows the resultant temperature thresholds for the thermal activation or inactivation to be used to identify their different roles so that the heat-driven biochemical reaction pathway could be mechanistically revealed. In summary, this study may provide an extensive structural basis for the optimal thermodynamic selectivity of not only thermophilic and hyperthermophilic enzymes in bacterial and archaeal species

but also other biological macromolecules. Further functional experiments are necessary to examine this structural basis so that the relevant engineering design rules can be developed to guide protein mutations to tune the thermal ring for novel biocatalysts or design of ligands for the specific recognition of regions that are key for thermostabilization and antibacterial or antifungal drugs.

■ ASSOCIATED CONTENT

Data Availability Statement

All data generated or analyzed during this study are included in this published article.

■ AUTHOR INFORMATION

Corresponding Author

    Guangyu Wang − *Department of Physiology and Membrane Biology, University of California School of Medicine, Davis, California 95616, United States;* Present Address: Department of Drug Research and Development, Institute of Biophysical Medico-chemistry, Reno, Nevada 89523, United States; ● orcid.org/0000-0002-5581-6926; Email: gary.wang10@gmail.com

Complete contact information is available at:
https://pubs.acs.org/10.1021/acsomega.3c03001

Author Contributions

G.W. wrote the main manuscript text, prepared Table [1], and Figures [1]−[9], and reviewed the whole manuscript.

Notes

The author declares no competing financial interest.

■ ACKNOWLEDGMENTS

■ CONVENTIONS AND ABBREVIATIONS

BaA, *Bacillus anthracis* fructose 1,6-bisphosphate aldolase; CFTR, cystic fibrosis transmembrane conductance regulator; CNA, constraint network analysis; DHAP, dihydroxyacetone phosphate; FBP, D-fructose 1,6-bisphosphate; EcA, *Escherichia coli* FBP aldolase; GBP, D-glucitol-1,6-bisphosphate; G3P, glyceraldehyde-3-phosphate; HpA, *Helicobacter pylori* FBP aldolase; MtA, *Mycobacterium tuberculosis* FBP aldolase; RINs, residue interaction networks; TaA, *Thermus aquaticus* FBP aldolase; T_m, melting temperature threshold; T_{th}, temperature threshold; WT, wild-type

■ REFERENCES

(1) Vieille, C.; Zeikus, G. J. Hyperthermophilic enzymes: sources, uses, and molecular mechanisms for thermostability. *Microbiol. Mol. Biol. Rev.* **2001**, *65*, 1−43.

(2) Freeze, H.; Brock, T. D. Thermostable Aldolase from Thermus aquaticus. *J. Bacteriol.* **1970**, *101*, 541−550.

(3) Karshikoff, A.; Ladenstein, R. Ion pairs and the thermotolerance of proteins from hyperthermophiles: a "traffic rule" for hot roads. *Trends Biochem. Sci.* **2001**, *26*, 550−556.

(4) Jacobs, D. J.; Rader, A. J.; Kuhn, L. A.; Thorpe, M. F. Protein flexibility predictions using graph theory. *Proteins* **2001**, *44*, 150−165.

(5) Vishveshwara, S.; Brinda, K. V.; Kannan, N. Protein structure: insights from graph theory. *J. Theor. Comput. Chem.* **2002**, *01*, 187−211.

(6) Radestock, S.; Gohlke, H. Protein rigidity and thermophilic adaptation. *Proteins* **2011**, *79*, 1089−1108.

(7) Pfleger, C.; Rathi, P. C.; Klein, D. L.; Radestock, S.; Gohlke, H. Constraint Network Analysis (CNA): a Python software package for efficiently linking biomacromolecular structure, flexibility, (thermo-)stability, and function. *J. Chem. Inf. Model.* **2013**, *53*, 1007−1015.

(8) Nutschel, C.; Fulton, A.; Zimmermann, O.; Schwaneberg, U.; Jaeger, K. E.; Gohlke, H. Systematically scrutinizing the impact of substitution sites on thermostability and detergent tolerance for bacillus subtilis lipase A. *J. Chem. Inf. Model.* **2020**, *60*, 1568−1584.

(9) Miotto, M.; Olimpieri, P. P.; Di Rienzo, L.; Ambrosetti, F.; Corsi, P.; Lepore, R.; Tartaglia, G. G.; Milanetti, E. Insights on protein thermal stability: a graph representation of molecular interactions. *Bioinformatics* **2019**, *35*, 2569−2577.

(10) Jonstrup, A. T.; Fredsøe, J.; Andersen, A. H. DNA Hairpins as Temperature Switches, Thermometers and Ionic Detectors. *Sensors* **2013**, *13*, 5937−5944.

(11) (a) Wang, G. The network basis for the structural thermostability and the functional thermoactivity of aldolase B. *BioRxiv* **2022**, DOI: 10.1101/2022.10.20.513014;(b) The network basis for the structural thermostability and the functional thermoactivity of aldolase B. *Molecules* **2023**, *28*, 1850.

(12) Wang, G. Network basis for the heat-adapted structural thermostability of bacterial class II fructose bisphosphate aldolase. *ACS Omega* **2023**, *8*, 17731−17739.

(13) Izard, T.; Sygusch, J. Induced fit movements and metal cofactor selectivity of class II aldolases: structure of Thermus aquaticus fructose-1,6-bisphosphate aldolase. *J. Biol. Chem.* **2004**, *279*, 11825−11833.

(14) Fonvielle, M.; Coinc, M.; Daher, R.; Desbenoit, N.; Kosieradzka, K.; Barilone, N.; Gicquel, B.; Sygusch, J.; Jackson, M.; Therisod, M. Synthesis and biochemical evaluation of selective inhibitors of class II fructose bisphosphate aldolases: towards new synthetic antibiotics. *Chem. - Eur. J.* **2008**, *14*, 8521−8529.

(15) Pegan, S. D.; Rukseree, K.; Franzblau, S. G.; Mesecar, A. D. Structural basis for catalysis of a tetrameric class IIa fructose 1,6-bisphosphate aldolase from Mycobacterium tuberculosis. *J. Mol. Biol.* **2009**, *386*, 1038−1053.

(16) Capodagli, G. C.; Sedhom, W. G.; Jackson, M.; Ahrendt, K. A.; Pegan, S. D. A noncompetitive inhibitor for Mycobacterium tuberculosis's class IIa fructose 1,6-bisphosphate aldolase. *Biochemistry* **2014**, *53*, 202−213.

(17) Jacques, B.; Coinc, M.; Sygusch, J. Active site remodeling during the catalytic cycle in metal-dependent fructose-1,6-bisphosphate aldolases. *J. Biol. Chem.* **2018**, *293*, 7737−7753.

(18) Floyd, R. W. Algorithm-97 - Shortest Path. *Commun. ACM* **1962**, *5*, 345.

(19) Qamar, S.; Marsh, K.; Berry, A. Identification of arginine 331 as an important active site residue in the class II fructose-1,6-bisphosphate aldolase of *Escherichia coli*. *Protein Sci.* **1996**, *5*, 154−161.

(20) Zgiby, S. M.; Thomson, G. J.; Qamar, S.; Berry, A. Exploring substrate binding and discrimination in fructose1, 6-bisphosphate and tagatose 1,6-bisphosphate aldolases. *Eur. J. Biochem.* **2000**, *267*, 1858−1868.

(21) Rutter, W. J. Evolution of Aldolase. *Fed Proc.* **1964**, *23*, 1248−1257.

(22) Kobes, R. D.; Simpson, R. T.; Vallee, R. L.; Rutter, W. J. Functional role of metal ions in a class II aldolase. *Biochemistry* **1969**, *8*, 585−588.

(23) Malay, A. D.; Procious, S. L.; Tolan, D. R. The temperature dependence of activity and structure for the most prevalent mutant aldolase B associated with hereditary fructose intolerance. *Arch. Biochem. Biophys.* **2002**, *408*, 295−304.

(24) Malay, A. D.; Allen, K. N.; Tolan, D. R. Structure of the thermolabile mutant aldolase B, A149P: Molecular basis of hereditary fructose intolerance. *J. Mol. Biol.* **2005**, *347*, 135−144.

(25) Lai, C. Y.; Nakai, N.; Chang, D. Amino acid sequence of rabbit muscle aldolase and the structure of the active center. *Science* **1974**, *183*, 1204−1206.

(26) Daher, R.; Coinçon, M.; Fonvielle, M.; Gest, P. M.; Guerin, M. E.; Jackson, M.; Sygusch, J.; Therisod, M. Rational design, synthesis and evaluation of new selective inhibitors of microbial class II (zinc dependent) fructose bisphosphate aldolases. *J. Med. Chem.* **2010**, *53*, 7836−7842.

(27) Dick, M.; Weiergräber, O. H.; Classen, T.; Bisterfeld, C.; Bramski, J.; Gohlke, H.; Pietruszka, J. Trading off stability against activity in extremophilic aldolases. *Sci. Rep.* **2016**, *6*, No. 17908.

(28) Liu, X.; O'Donnell, N.; Landstrom, A.; Skach, W. R.; Dawson, D. C. Thermal instability of ΔF508 CFTR channels function: protection by single suppressor mutations and inhibiting channel activity. *Biochemistry* **2012**, *51*, 5113−5124.

(29) Wang, G. Interplay between inhibitory ferric and stimulatory curcumin regulates phosphorylation-dependent human cystic fibrosis transmembrane conductance regulator and ΔF508 activity. *Biochemistry* **2015**, *54*, 1558−1566.

(30) Wang, G. Molecular basis for Fe(III)-independent curcumin potentiation of cystic fibrosis transmembrane conductance regulator activity. *Biochemistry* **2015**, *54*, 2828−2840.

(31) Wang, G.; Linsley, R.; Norimatsu, Y. External Zn^{2+} binding to cysteine-substituted cystic fibrosis transmembrane conductance regulator constructs regulates channel gating and curcumin potentiation. *FEBS J.* **2016**, *283*, 2458−2475.

(32) Karshikoff, A.; Nilsson, L.; Ladenstein, R. Rigidity versus flexibility: the dilemma of understanding protein thermal stability. *FEBS J.* **2015**, *282*, 3899−3917.